Journal of Materials Chemistry A

Optimizing semiconductor thin films with smooth surfaces and well-interconnected networks for high-performance perovskite solar cells

Journal:	*Journal of Materials Chemistry A*
Manuscript ID	TA-ART-05-2016-004053.R1
Article Type:	Paper
Date Submitted by the Author:	06-Jul-2016
Complete List of Authors:	Wu, Wu-Qiang; The University of Melbourne, School of Chemistry Chen, dehong; Melbourne University, School of Chemistry Huang, Fuzhi; Monash University, Materials Science and Engineering Cheng, Yi-Bing; Monash University, Materials Engineering Caruso, Rachel; The University of Melbourne, School of Chemistry; CSIRO, Manufacturing

Journal of Materials Chemistry A

ARTICLE

Optimizing semiconductor thin films with smooth surfaces and well-interconnected networks for high-performance perovskite solar cells†

Received 00th January 20xx,
Accepted 00th January 20xx

DOI: 10.1039/x0xx00000x

www.rsc.org/

Wu-Qiang Wu,[a] Dehong Chen,[a]* Fuzhi Huang,[b] Yi-Bing Cheng[c]* and Rachel A. Caruso[a,d]*

An efficient solution-based technique to grow homogeneous TiO_2 nanoparticle (TNP) thin films with tunable crystal size, porosity and roughness on a transparent conducting oxide (TCO) substrate is demonstrated that can direct the evolution of an optimal perovskite morphology. Combining a gas-assisted spin-coating and a subsequent blended vapor-assisted annealing protocol, highly crystalline perovskite films with a flat surface, reduced pin-holes and micrometer-scale grains were formed. The blended vapor was produced from a mixed N,N-dimethylformamide (DMF) and chlorobenzene (CBZ) solution. In the mixed vapor-assisted annealing, the DMF vapor molecules dissolved small perovskite grains and the anti-solvent CBZ facilitated rapid precipitation of perovskite crystals filling the gaps and pores among adjacent grains to produce high quality perovskite films. Perovskite solar cells with consistent power conversion efficiencies exceeding 15% and little cell-to-cell variability have been obtained. This work shows that fine tuning of the semiconducting networks by simple chemistry methods, can potentially lead to the fabrication of high-performance and cost-effective thin film solar cells.

Introduction

The rapid development of perovskite solar cells (PSCs) has evoked widespread scientific and industrial interest, owing to the advantages of inexpensive materials and simple solution-processable fabrication techniques, as well as surging device performances.[1] High power conversion efficiencies (PCEs) of around ~15-16% have been achieved on both mesoporous and planar heterojunction structured devices within a short time,[2-4] and a PCE of 22.1% has been certified.[5]

Generally, in mesoporous structured PSCs, the charge separation and electron transport take place in two different semiconducting layers, namely, the perovskite ($CH_3NH_3PbX_3$, X=Cl, Br, I) semiconductor layer and the metal oxide electron transport layer (ETL).[6, 7] In this case, the porous metal oxide film anchors the light absorbing perovskite, and often a solid self-standing perovskite capping layer is also formed on the infiltrated mesoporous anode scaffold. This bilayer structure, which integrates the advantages of both the mesoscopic and planar structure has proven to be crucial for achieving high-performance PSCs with high reproducibility.[8] As the perovskite thin films are deposited on ETL scaffolds to fabricate the devices, the impact of the ETL morphology (pore size, surface area and roughness) on the perovskite crystal growth and film formation should be scrutinized.[9-12] For example, it is still challenging to form a smooth and continuous mesoporous TiO_2 nanoparticle (TNP) thin film that covers the TCO substrate well; a requirement for achieving the subsequent homogeneous perovskite film coverage. However, this topic has not been extensively explored for mesoscopic PSCs.

In addition to optimizing the ETL, delicate control of the structure, grain size and crystallinity of the perovskite capping layer is also critical to reduce interfacial recombination losses and thus realize high-performance devices.[13] In general, the relatively poor solubility of perovskite in DMF, the conventional one-step solution-casting or sequential dip coating procedures, and the fast perovskite crystallization with solvent evaporation upon thermal annealing led to non-continuous films with large morphological variations, where pinholes can introduce shunting and thus limit the cell performance.[14, 15] Hence, recent efforts have been focused on improving the perovskite film surface coverage by increasing the crystal size and improving the crystalline quality of the grains, *e.g.* with additives,[16] solvent washing,[8, 17] varying the solution composition and concentration,[18, 19] changing the organic anion

[a]*Particulate Fluids Processing Centre, School of Chemistry, The University of Melbourne, Melbourne, Victoria 3010, Australia. *Email - rcaruso@unimelb.edu.au, dehongc@unimelb.edu.au*
[b]*State Key Laboratory of Advanced Technology for Materials Synthesis and Processing, Wuhan University of Technology, Wuhan, 430070, China*
[c]*Department of Materials Science and Engineering, Monash University, Victoria 3800, Australia.*Email - yibing.cheng@monash.edu*
[d]*CSIRO Manufacturing, Private Bag 10, Clayton South, Victoria 3169, Australia*
†Electronic Supplementary Information (ESI) available: See
DOI: 10.1039/x0xx00000x

components,[20] or controlling the annealing time, temperature, humidity, and atmosphere.[21-24]

Previously, we developed an effective gas-assisted one-step perovskite spin-coating method that speeds up the evaporation of the solvent. This accelerates supersaturation of the solution, and also facilitates the diffusion and infiltration of perovskite molecules into the mesostructured support; thus resulting in uniform perovskite films with very few pinholes.[23] Recently, Huang and co-workers developed a solvent annealing method to increase the perovskite crystallinity and grain size, further improving the device performance. In this method, DMF vapor was introduced during the crystallization of the perovskite materials, which facilitates the diffusion of precursor ions and molecules and thus promotes grain growth and yields a larger grain size.[21]

Herein, a hydrothermal technique has been applied to coat the fluorine-doped tin oxide (FTO) substrates with films of TiO_2 nanoparticles (TNPs) having controllable particle size and uniformity. The perovskite film was then coated on these FTO/TNP substrates via the gas-assisted spin-coating approach. The optimized TNP (~25 nm in particle size) thin film significantly improved the uniformity of the $CH_3NH_3PbI_3$ film due to the smooth TNP film surface. In addition, a vapor-assisted annealing step employing an optimized blend of DMF and CBZ was applied to obtain a highly crystalline perovskite film with a flat surface and reduced pinholes due to the accelerated dissolution-precipitation-crystallization process in the presence of CBZ anti-solvent. Since DMF and CBZ have similar boiling points, the mixed vapor would be expected to affect the reconstruction and crystallization process uniformly across the films. The optimized perovskite morphology correlates to the solar cell performance. By optimizing the device fabrication conditions, a PCE of 15.77% for PSCs under one sun illumination was achieved. Additionally, the role of the morphologically controlled semiconductor network on the device optimization and the development of highly efficient PSCs have been clarified.

Experimental Section

FTO/TNP Substrate Preparation. The laser-patterned FTO substrates (TEC8, Dyesol) were cleaned sequentially in an ultrasonic bath with soap (5% Hellmanex in water), Milli-Q water, ethanol and acetone, each for 15 min. The TNP thin films were hydrothermally grown on FTO glass substrates without the assistance of a seed layer. To avoid the growth of TNPs on the glass side of FTO substrate, the glass side was covered with Kapton tape before the hydrothermal reaction. The precursor solution was prepared by dissolving the potassium titanium oxide oxalate dihydrate (PTO, Sigma-Aldrich) in Milli-Q water at concentrations of 1.7 mM to 28.0 mM. The cleaned FTO substrate (2×1 cm^2) was immersed in the Teflon container of an autoclave (50 mL in volume) containing 20 mL precursor solution with the FTO side facing down at an angle of 45 °, and the autoclave was sealed and heated at 150 °C for 6 h. After cooling to room temperature, the TiO_2 thin films were rinsed with Milli-Q water and ethanol several times, and the Kapton tape was removed and the glass side was washed using absolute ethanol. Then the as-prepared films were annealed at 500 °C for 3 h in air to crystallize the TiO_2 and remove any residual organic solvent. As a reference, a mesoporous TiO_2 (mp-TiO_2) layer was deposited on a FTO glass substrate by spin coating at 3000 rpm for 30 s using a TiO_2 paste (PST-30 NRD, CCIC-JGC, Japan) diluted in ethanol (1:4 in weight ratio), followed by calcination on a hot plate at 150 °C for 30 min. The electrodes were soaked in 20 mM $TiCl_4$ aqueous solution at 70 °C for 30 min and then rinsed with Milli-Q water followed by annealing at 500 °C for another 30 min.

Perovskite Solar Cell Fabrication. To generate the $CH_3NH_3PbI_3$ perovskite solution, PbI_2 (Sigma-Aldrich) and CH_3NH_3I (home-made) were dissolved in an anhydrous DMF (Sigma-Aldrich) solution at a molar ratio of 1:1 with final concentration of ~45 wt%. The gas-assisted method was used to deposit uniform perovskite films in a nitrogen-filled glovebox.[23] The $CH_3NH_3PbI_3$ solution was spin-coated on top of the FTO/TNP substrate at room temperature at 6500 rpm and after 2 s a dry argon gas stream (60 psi) was blown over the film for 10 s to accelerate the perovskite nucleation and crystallization; the film was spun for another 30 s. The films were then annealed under an ambient or vapor atmosphere at 100 °C for 1-40 min. To treat the perovskite films with vapor annealing, the films were placed on top of a hot plate (set at 100 °C unless otherwise specified) and covered by a glass petri dish (3.5 cm in diameter). Around 10 μL DMF, DMF:CBZ=2:1 (volume ratio), DMF:CBZ=1:1 (volume ratio), DMF:CBZ=1:2 (volume ratio) or CBZ (Sigma-Aldrich) was added at the edge of the petri dish, so that the DMF, blended DMF:CBZ or CBZ vapor can diffuse into the perovskite film. The solution for HTM coating was prepared by dissolving 41.6 mg spiro-MeOTAD (Taiwan, Lumtec) in 0.5 mL CBZ, in which 7.5 μL (lithium bis(trifluoromethylsulphonyl)imide in acetonitrile (500 mg mL-1) and 14.4 μL 4-tert-butylpyridine (Sigma-Aldrich) were added. Spiro-MeOTAD was deposited at 3000 rpm for 30 s. Finally, an 80 nm-thick gold layer was thermally evaporated on top of the device as a back contact.

Characterization. The morphological features of the TiO_2 and perovskite films were examined by a field emission scanning electron microscope (FE-SEM, Quanta 200F FEI). The atomic force microscopy (AFM) images were obtained using a Cypher instrument (Asylum Research Company) in "tapping" mode and scanning over a range of 5×5 μm^2. The surface roughness was measured as the root mean squared (RMS) roughness over the scanning area. Crystallinity and phase identification of the products was conducted using X-ray diffraction (XRD, Bruker D8 Advance Diffractometer) equipped with Cu Kα radiation (λ=1.5418 Å). The transmittance and absorbance of the electrodes were obtained with a UV-vis-NIR spectrophotometer (Lambda 1050, Perkin-Elmer).

Photocurrent-photovoltage (*J-V*) curves were measured using a Keithley 2400 source meter under AM 1.5G illumination (100 mW cm^{-2}) provided by an Oriel solar simulator. The incident light intensity was calibrated with a silicon photodiode (Peccell Technologies). The solar cells were masked with a metal aperture to define the active area, typically 0.16 cm^2. The IPCE spectra were recorded as a function of wavelength from 380 to 800 nm on a Keithley 2400 source meter under the irradiation of a 300 W xenon lamp fitted with an Oriel Cornerstone^{TM} 260 1/4 m monochromator. The photoluminescence spectra were obtained on a FluoroMax-4 Spectrofluorometer as a function of emission wavelength from 650 to 850 nm. The excitation wavelength was set at 460 nm.

Results and Discussion

The ability to control the morphology of the individual components within the PSC and the optimization of interfacial interactions between the layers are two highly important factors for enhancing the efficiency of these solar cells. Controlling the titania nanoparticles through careful chemical syntheses varies the film morphology and thus will influence the perovskite crystallization. Additional engineering of the conditions under which the perovskite layer is annealed can be carried out to give high quality perovskite films. These two approaches were examined here for the construction of photovoltaic devices with improved efficiency.

A highly controllable hydrothermal technique was used to grow ultrathin TiO_2 films on FTO glass as the ETL for PSC application. The sketch in Fig. S1 shows the simple approach to fabricate TNP thin films that cover the FTO glass well using a hydrothermal solution containing the potassium titanium oxide oxalate dihydrate (PTO) in Milli-Q water. The bare FTO consists of submicrometer sized FTO crystals with a pyramid shape; this rough surface makes it challenging to fully cover via the conventional solution-casting method. The high-magnification SEM images in Fig. 1a and 1c show the morphologies of the TNP films prepared using different concentrations of PTO. The TNP coatings replicate the pristine FTO crystal morphology, indicating the formation of thin films in a highly controlled manner. The uniform particle distribution and coverage can be attributed to their oriented attachment onto the FTO surface via a bottom-up mechanism during the hydrothermal process.[25] The degree of TNP coverage correlates to the PTO concentration. Typically, the TiO_2 particle size slightly increases with increasing PTO concentration and the best surface coverage was observed for the PTO-14 mM sample (Fig. 1c and Fig. S2). When a low PTO concentration was used, thin TNP films were formed, while the higher PTO concentration led to increased film thickness, that generated some mesoporous structure. Note that some low-lying gaps on the FTO surface have not been filled by the small nanoparticles at a low PTO concentration of 1.7 mM (Fig. 1a and Fig. S2b). The surface roughness of the TNP films can be measured using AFM in tapping mode. As shown in Fig. S3, the root-mean-squared (RMS) roughness of the films decreased from 53 to 34 nm for films prepared with PTO concentrations from 1.7 to 14 mM. The PTO-14 mM sample exhibited the smoothest surface. The XRD pattern, Fig. S4, indicates the anatase phase in the

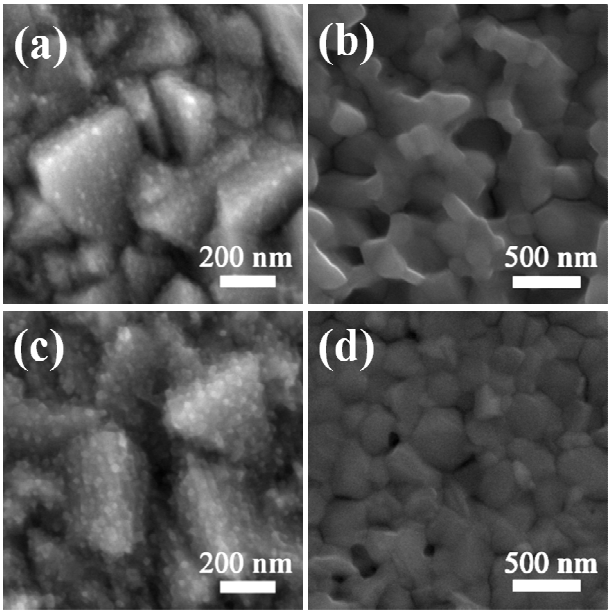

Fig. 1 SEM images of the surface morphologies of the (a, c) FTO/TNP substrates prepared using different PTO concentrations and (b, d) corresponding FTO/TNP/$CH_3NH_3PbI_3$ films: (a, b) PTO-1.7 mM and (c, d) PTO-14 mM.

PTO-14 mM film with observable (101) and (200) reflections (JCPDS 21-1272).

The optical properties of the TiO_2 thin film play a critical role in the solar cell performance, which can be identified from the UV-Vis transmittance spectra in Fig. S5. The TiO_2 nanoparticle coating has some anti-reflective effect, Fig. S5a, in which the FTO/TNP films exhibited improved transmittance compared to that of the bare FTO glass (*e.g.* an increase of ~2.8-4.7% at 550 nm, Fig. S5b). The improved transparency of the films would increase the fraction of incident solar light that enters the perovskite light absorbing layer, resulting in an improved light harvesting efficiency and thus PCE.[26]

The effect of the different TNP thin films on the morphology of the $CH_3NH_3PbI_3$ film fabricated via the gas-assisted one-step spin-coating and conventional thermal annealing procedures was investigated. As is the case for the mesoscopic solar cell, the $CH_3NH_3PbI_3$/DMF solution will infiltrate into the nanopores of the TNP film, while at the same time a perovskite capping layer will be formed on top.[8, 19, 27, 28] The grain size of the $CH_3NH_3PbI_3$ in the mesoporous host is generally believed to be limited by the pore size of the TNP film, though there is crystal growth of the $CH_3NH_3PbI_3$ grains on top of the mesoporous scaffold.[19] As is shown in Fig. 1b, 1d and Fig. S6, the number of pinholes reduced, as the FTO/TNP became smoother (from PTO-1.7 mM to PTO-14 mM). The perovskite morphology on the PTO-1.7 mM film is mostly tetragonal-like discrete crystals that are randomly distributed and poorly interconnected (with size varying between 100-250 nm, Fig. 1b

and Fig. 2a); whereas on top of the PTO-14 mM film, tabular-like grains with less sharp edges and thus flatter surfaces are obtained (with crystal size varying between 250-500 nm, Fig. 1d and Fig. 2b). A shorter charge carrier transport distance between perovskite crystals or from perovskite to TiO_2 can be expected in PSCs containing compact and smooth perovskite films when compared with those possessing a porous and rough perovskite structure,[24, 29] as shown in Fig. 2a and 2b.

From the cross-sectional SEM images (Fig. S7), the perovskite formed on top of the PTO-1.7 mM TNP thin film consists of two layers of small perovskite crystals and voids, with a high crystal surface roughness (Fig. S7a), which would expose some of the TiO_2 particles. As a result, the hole-transporting material (HTM) can penetrate through the pinholes in the perovskite layer and come in contact with the bare TiO_2, leading to charge recombination (Fig. S7b). However, on the PTO-14 mM TNP thin film, the perovskite layer is more compact with larger monolayer grains and a reduced number of pinholes (Fig. S7c). Consequently, the perovskite layer serves as a barrier for separating the HTM and the TiO_2 blocking layer, which would reduce charge recombination (Fig. S7d).[27]

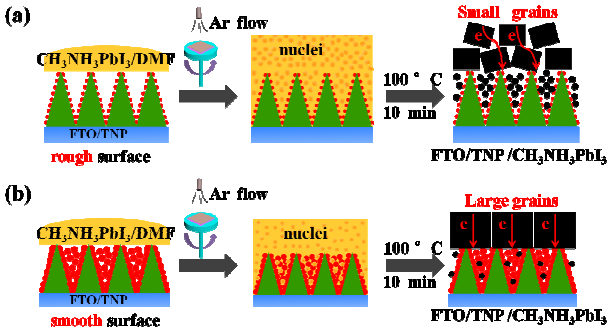

Fig. 2 Sketch showing the perovskite film formation and the electron transport behavior on (a) FTO/TNP with rough surface (PTO-1.7 mM) and (b) FTO/TNP with smooth surface (PTO-14 mM). Note: the red spots represent the TiO_2 nanoparticles.

In order to investigate the effect of different TNP thin films on the device performance, PSCs were fabricated using different TNP ETLs with a device structure of FTO/TNP/$CH_3NH_3PbI_3$/spiro-MeOTAD/Au. As shown in Fig. S8 and Table S1, the PSCs based on FTO/TNP electrodes prepared with a larger amount of PTO exhibited an enhanced PCE, increasing from 5.55% for the PTO-1.7 mM sample to 12.08% for the PTO-14 mM sample. An improvement in all the device parameters was observed, e.g. J_{sc} increased from 15.31 to 19.85 mA cm^{-2}, V_{oc} from 751 to 942 mV and *FF* from 0.48 to 0.65. This can be attributed to the improved light harvesting efficiency, superior charge carrier transport capability as well as suppressed charge recombination for the FTO/TNP (PTO-14 mM)/$CH_3NH_3PbI_3$ films with better surface coverage.

Although the optimal TNP morphology (PTO-14 mM) has led to improved perovskite coverage, it is not totally compact. It is generally believed that the pinhole-free perovskite films with high crystalline properties are important for highly efficient PSCs.[30, 31] To optimize the perovskite film morphology, a mixed vapor-assisted annealing following the gas-assisted one-step spin-coating process was applied on top of the PTO-14 mM~~using the vapor-assisted annealing technique for different solvent ratios~~, as shown in Fig. 3. The ~~crystal~~ grain structures obtained using the vapor-assisted annealing technique for different solvent ratios can be seen in Fig. 4a-c. The conventional thermal annealing delivered a porous crystalline perovskite film (Fig. 1d), whereas following the vapor-assisted annealing a considerably different morphology was attained with almost a full surface coverage on the substrates with larger crystalline grains, reduced pinholes and also relatively smooth surface. Typically, the perovskite films were annealed with DMF or a DMF-CBZ mixture at 100 °C for 30 min. Since the perovskite is soluble in DMF, the presence of DMF vapor could provide a moist environment that allows for prolonged growth of the perovskite crystals, thus yielding large grains.

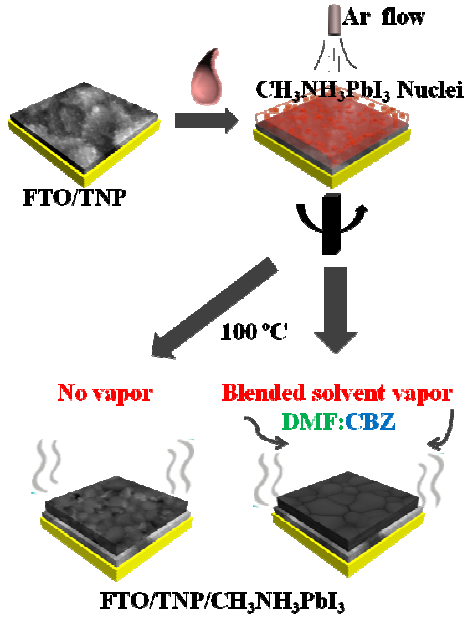

Fig. 3 Schematic of the combined gas-assisted spin-coating and vapor-assisted annealing procedures used to optimize the perovskite semiconductor morphology. The $CH_3NH_3PbI_3$/DMF solution was spin-coated onto the FTO/TNP substrate under Ar gas to accelerate solvent evaporation, followed by either conventional thermal annealing (No vapor) or blended vapor-assisted annealing.

Adding an anti-solvent, such as CBZ, into the perovskite solution during the spin-coating process induces fast nucleation and crystallization of the perovskite and thus formation of large grains with full surface coverage.[17] Herein, the DMF and CBZ mixed vapor has been used to facilitate the crystal growth and construct a uniform film in a fast manner. The vapor composition was varied, altering the in-plane grain size distribution, Table S2, which ranged from a few hundred nanometers to a micrometer in size. Increasing the CBZ in the mixed vapor is beneficial as it increases the crystal size, reduces the pinholes and results in a smoother perovskite surface. The perovskite film produced with DMF:CBZ=1:1 (by volume) vapor is extremely compact, pinhole-free and has good surface coverage (Fig. 4c). Further increasing the CBZ volume (>50%) will decrease the grain size, and pure CBZ does not

result in a high-quality perovskite film (Fig. S9). The films fabricated using different annealing conditions were characterized by AFM as shown in Figure S10. The RMS roughness of the perovskite films annealed without additional vapor (no vapor), or with DMF, DMF:CBZ=2:1 and DMF:CBZ=1:1 were 48, 44, 36 and 30 nm, respectively, for areas of 5×5 μm^2. The roughness of the films fabricated via the vapor annealing is reduced compared with the conventional thermal annealing process. The smoother perovskite film is generally believed to decrease the possibility of short-circuiting within the device as a flat HTM layer can fully cover the perovskite film, preventing contact between the Au electrode and the perovskite.[20, 27]

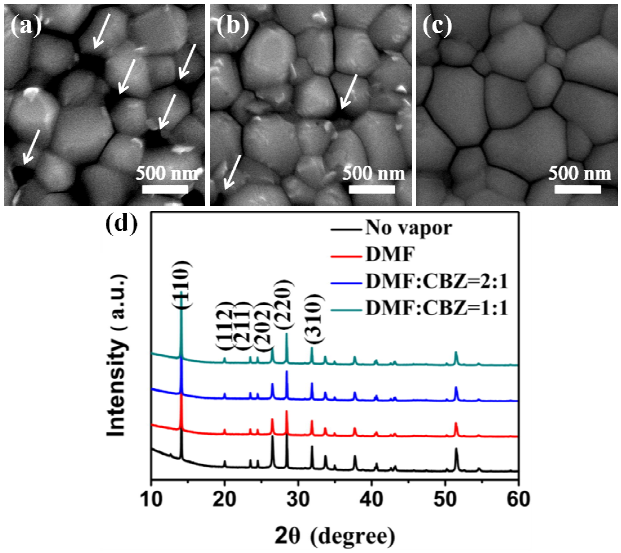

Fig. 4 SEM images of the perovskite films prepared using the vapor-assisted annealing of (a) DMF, (b) DMF:CBZ=2:1 (by volume) and (c) DMF:CBZ=1:1 (by volume) as solvents at 100 °C for 30 min. White arrows in the SEM images indicate the existence of pin-holes in the film. (d) XRD patterns of the different vapor annealed perovskite films.

X-ray diffraction patterns of the perovskite films fabricated with or without vapor annealing are shown in Fig. 4d. The strong Bragg peaks at 14.08 º, 28.41 º, and 31.85 º for all four samples can be assigned to the (110), (220), and (310) diffractions of the $CH_3NH_3PbI_3$ crystal,[32] indicating that the vapor-assisted annealing does not change the crystal phase. All of the XRD diffraction peaks of the vapor annealed films were slightly sharper than those of the non-vapor annealed films, suggesting increased crystallinity with larger grain size and less grain boundaries after the annealing. All these samples were stored in an ambient environment for seven-days, and then further investigated using X-ray diffraction. As shown in Fig. S11, an obvious PbI_2 peak at 12.56 º can be observed for all samples due to the reaction of the perovskite with moisture in the atmosphere. However, the PbI_2 peak intensity gradually decreased in the order of no-vapor>DMF>DMF:CBZ=2:1> DMF:CBZ=1:1, indicating that the vapor-annealing treatment retards the degradation of the film (possibly due to the highly crystalline perovskite film formed), which is significant for future commercialization.

The synergistic effects exerted by the presence of DMF and CBZ vapor on the perovskite crystal growth merit attention. The perovskite film formation using different solvent ratios was compared under the same annealing temperature and time (100 °C for 5 min). As shown in Fig. 5a-5c, the vapor-assisted annealing procedure densifies the perovskite crystal networks to different degrees depending on the vapor. Mixing CBZ and DMF has increased the grain size and smoothed the perovskite surface. This indicates that the introduction of CBZ could accelerate the dissolution–precipitation process. In the case of pure DMF vapor annealing (Fig. 5a), the perovskite crystals formed in the initial spin-coating would to some extent be dissolved by the added DMF vapor, which would also slow the DMF evaporation from the spin-coating step, thus forming larger grains. However, in the case of the DMF:CBZ=1:1 mixed solvent vapor annealing treatment (Fig. 5c), the DMF vapor would dissolve the smaller irregular perovskite crystals, while simultaneously the CBZ vapor, serving as an anti-solvent, would facilitate supersaturation, thus constructing well-interconnected perovskite crystals with large grain size more rapidly. It is believed that the vapor would preferentially dissolve the small grains with rough surfaces, causing mass transport towards the low-lying gaps, filling the voids and pores among adjacent crystals, producing smooth surfaces. This process would lead to grain coarsening,[13] in which the small grains shrink and are gradually eliminated, resulting in a well-interconnected grain network with large crystals and smooth surface. Moreover, the addition of CBZ to the vapor may vary the vapor pressure of DMF, thus DMF could be diluted by CBZ to an optimal concentration or amount for film formation. Fig. 5d illustrates crystal growth and evolution of the perovskite film from crystals (undulating and non-continuous in their coverage) to tabular-like grains (flatter and more connected when annealed) with mixed solvent (DMF:CBZ=1:1) vapor annealing. It is worth noting that the general principle for choosing the appropriate solvent to match the DMF aprotic solvent should be that it can be dissolved in DMF but does not dissolve perovskite or make it decompose. In addition, an anti-solvent with low boiling point or vapor pressure is preferable.

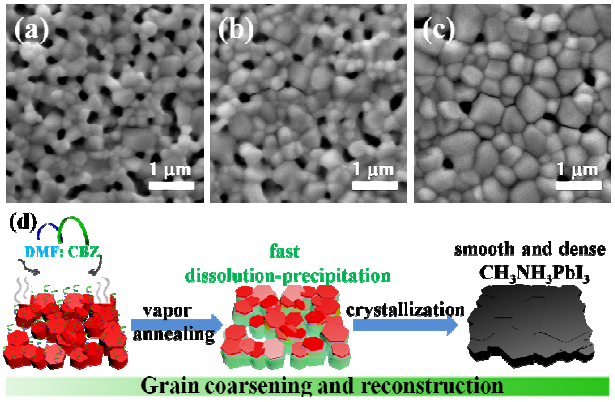

Fig. 5 SEM images of different vapor annealed perovskite films prepared using (a) DMF, (b) DMF:CBZ=2:1 and (c) DMF:CBZ=1:1 at 100 °C for 5 min. (d) Schematic representation of the crystal growth and evolution of the blended-solvent (DMF:CBZ=1:1) vapor annealed perovskite film.

The grain growth was studied by varying the annealing time from 1 to 40 min at 100 °C for the optimized vapor condition (DMF:CBZ=1:1). SEM surface images are shown in Fig. S12 and the grain size distribution is summarized in Table S2. The grain size increases with increased annealing time. The perovskite films evolved from polycrystalline (100-400 nm) with numerous pinholes (1 min, Fig. S12a), to compact and continuous films containing well-connected large grains (300-1000 nm) without pinholes (40 min, Fig. S12f). The crystal growth and evolution is fast in the first 20 min, and then slowed with further annealing time due to consumption of the precursor.[21] The mixed vapor annealed perovskite film has less grain boundaries leading to more efficient charge carrier transport in the large single grains.[31] According to Fig. S12, the optimized annealing time for DMF:CBZ = 1:1 is 30 min. The effect of annealing time on the perovskite film fabricated using the other blended solvent conditions, DMF:CBZ = 2:1 and DMF:CBZ = 1:2, was studied, Fig S13. Under these conditions a prolonged annealing time (>30 min) leads to an improved quality of the perovskite films with reduced pinholes and a much smoother surface. The optimized annealing time is 60 min for DMF:CBZ = 2:1 (Fig. S13b, RMS=32 nm) and 120 min for DMF:CBZ = 1:2 (Fig. S13f, RMS=35 nm), as shown in Fig. S13, Fig. S14 and Table S2. The equal volume of DMF and CBZ (DMF:CBZ=1:1) would synergistically balance the dissolution-precipitation process, leading to the formation of well-interconnected perovskite films with large grains. However, excess DMF (DMF:CBZ=2:1) would dissolve more of the perovskite film (dissolution outperforms the precipitation), and thus requires a longer annealing time (60 min) to reshape the film morphology. In the case of excess CBZ (DMF:CBZ=1:2), an extra-long annealing time is needed (120 min). The perovskite dissolution in the smaller amount of DMF vapor would precipitate quickly in the presence of a larger amount of CBZ (anti-solvent), which in turn, results in the fact that the pore-healing is not that effective when the annealing time is less than 90 min for DMF:CBZ = 1:2 (Fig. S13d and S13e). Moreover, increasing the annealing temperature facilitated vapor diffusion within the perovskite film, thus was conducive to construct perovskite films with large grains and smooth surfaces more rapidly (Fig. S15).

Cross-sectional SEM images in Fig. S16 show two representative devices fabricated without (no vapor) or with vapor annealing (DMF:CBZ=1:1). Both of the perovskite films have well-defined grains across the film thickness. The average grain sizes of the no vapor film (Fig. S16a) are only slightly larger or comparable to the perovskite film thickness. However, for the mixed vapor annealed film, the in-plane grain sizes are significantly larger than the film thickness, which would greatly enhance the charge extraction properties due to efficient charge carrier transport in the large single grains without frequently encountering grain boundaries, defects and impurities before being collected (Fig. S16b).

To determine the role of the perovskite morphology on the cell performance, PSCs employing the perovskite films prepared under the different thermal annealing conditions were fabricated, see results in Fig. 6 and Table 1. The devices were structured as FTO/TNP (80 nm)/$CH_3NH_3PbI_3$ (350 nm)/spiro-MeOTAD (150 nm)/Au (80 nm). Clearly, the vapor annealed films yielded higher J_{sc}, V_{oc} and *FF* than the conventional annealed film (referred to as no vapor, Fig. 6a and Table 1). This can be attributed to the improved perovskite film coverage, with increasing grain size and decreased number of grain boundaries, achieved by using the vapor annealing process. The composition of the vapor impacted on the grain sizes of the perovskite and thus the photovoltaic performance. The optimized solvent ratio is DMF:CBZ=1:1 for the annealing process, where a PCE of 15.77% was achieved. The impressively high J_{sc} is likely to stem from the optimized perovskite film morphology consisting of larger grain sizes, high crystallinity, and excellent surface coverage. This enhanced the light absorption and thus LHE, as shown in the incident-photon-to-current conversion efficiency (IPCE) curves in Fig. 6b. The use of the vapor annealed perovskite film noticeably improved the IPCE over the wavelength region from 380 to 800 nm (Fig. 6b). The IPCE was above 80% across the wavelength region from 400 nm to 750 nm for the PSCs based on the perovskite film prepared via DMF:CBZ=1:1 vapor annealing. The integrated J_{sc} obtained from the IPCE for this cell is 21.22 mA cm^{-2}, which is consistent with the J_{sc} from *J-V* curves. This indicates an excellent incident photon collection capability of the cell containing the well-interconnected, large perovskite grains with sufficient surface coverage, thus yielding a higher J_{sc}.[22, 33]

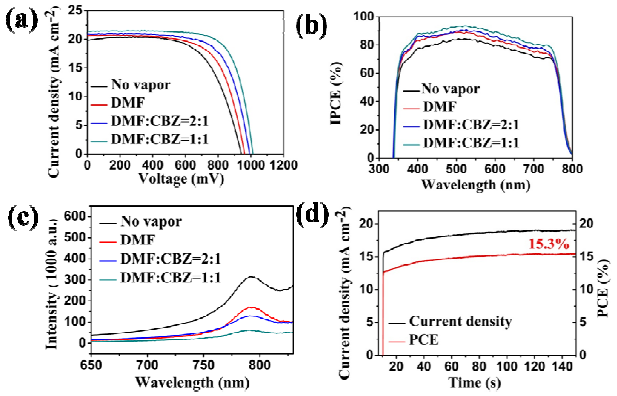

Fig. 6 (a) *J-V* curves and (b) IPCE spectra of PSCs containing perovskite films fabricated under different thermal annealing conditions. (c) Photoluminescence spectra of the different perovskite films deposited on Glass/TNP substrates (excitation at 460 nm). (d) Photocurrent density and power conversion efficiency measured as a function of time for the best-performing cell (DMF:CBZ=1:1) held at a forward bias at the point of maximum power output (0.80 V). The cell was kept in the dark prior to the start of the measurement.

Table 1. Photovoltaic characteristics of the PSCs constructed using $CH_3NH_3PbI_3$ films fabricated using different thermal annealing conditions under one sun illumination (AM 1.5 G, 100 mW cm^{-2}).

PSCs	J_{sc} (mA cm^{-2})	V_{oc} (mV)	η (%)	*Average* η (%)	*FF*
No vapor	19.85	942	12.08	11.45±0.35	0.65
DMF	20.60	962	13.20	12.58±0.40	0.67
DMF:CBZ=2:1	20.91	992	14.32	13.65±0.38	0.69
DMF:CBZ=1:1	21.44	1013	15.77	15.25±0.41	0.73

** data for average PCE (η) are calculated from at least 10 devices.*

The V_{oc} (942 mV) is lower for the no vapor-annealed devices. This can be explained by increased shunting because of the presence of numerous pinholes in the noncontinuous perovskite film that can lead to direct contact between *spiro*-MeOTAD and the TNP ETL.[20, 29] The V_{oc} improvement for the vapor annealed films originates from the formation of a compact and uniform perovskite capping layer. There are two major benefits in optimizing the perovskite film morphology: i) larger grains have less bulk defects and higher charge mobility, allowing for the photogenerated carriers to propagate through the device and be effectively extracted without frequently encountering grain boundaries, defects and impurities; and ii) the reduced interfacial areas associated with large grains suppress charge trapping and thus reduce the recombination loss.[21, 31] The suppressed charge recombination is expected to contribute to the increase in V_{oc} and device performance. This was confirmed with the photoluminescence (PL) spectra of the perovskite films prepared under different thermal annealing conditions on glass/TNP substrates (Fig. 6c). Similar absorption edges and sharp PL spectra at ~780 nm were observed for all samples. Notably, the contact of larger perovskite crystals with TNP significantly accelerates the PL quenching compared to the small polycrystalline perovskite analogues. The quenching effect is most obvious in the DMF:CBZ=1:1 case, indicating that the charge extraction at this TNP/perovskite interface is most efficient and effective, which is largely driven by the optimized perovskite semiconductor morphology. The coverage of the TNP ETL with densely interconnected perovskite crystals (DMF:CBZ=1:1) can effectively avoid undesired charge recombination. Moreover, the low exciton binding energy of the continuous upper perovskite layer will be beneficial for the dissociation of excitons into free carriers and thus would be expected to improve charge transfer,[27] which is reflected in the observed high V_{oc} of 1013 mV. In addition, the FF increased from 0.65 (no vapor) to 0.73 (DMF:CBZ=1:1). The increased *FF* results from compact and uniform perovskite films formed by the vapor annealing approach, leading to the balanced hole-electron transport and reduced charge recombination.[34] Also, the compact perovskite capping layer (DMF:CBZ=1:1), allows excellent coverage of the HTM on top of the perovskite film, thus ensuring the improved *FF*.

The hysteresis in the *J-V* curves is an issue for accurately evaluating the performance of PSCs,[35-37] therefore the device prepared using the DMF:CBZ=1:1 vapor annealed film was measured with change in the scanning rates and scanning directions. The variation in efficiency is small (PCE decreases from 15.77% to 14.97% when the scan rate increases from 0.1 to 0.5 V s^{-1}, Fig. S17), reflecting that the cell reaches an equilibrium state and its output is very close to the real value. The *J-V* curves obtained with forward and reverse scanning directions (Fig. S18) show that there is little hysteresis. Hence, it is necessary to monitor the stabilized power output under load near the point of maximum power. The steady-state photocurrent output was measured at the voltage giving maximum power (0.80 V). As shown in Fig. 6d, the photocurrent rose to a relatively stable value, and the steady-state current was similar to that measured from the photocurrent scanning, yielding a stabilized PCE around 15.3%. The slight increase in photocurrent and PCE in the 150 s may be caused by the light-soaking effect.[38] To investigate the reproducibility of the results, a batch of 10 cells were tested and the photovoltaic parameters of these PSCs are tabulated in Table S3. An average PCE of 15.25±0.41% was observed. This small standard deviation indicates good device reproducibility and again confirms the notably high PCE of the PSCs based on the optimized semiconducting networks (both TiO_2 ETL and $CH_3NH_3PbI_3$ light absorber). The short-term stability of the unencapsulated cell was checked; the PCE can be maintained at ~15.04% (J_{sc}=21.23 mA cm^{-2}, V_{oc}=971 mV and FF=0.73) after seven-days storage in an ambient dry air environment. The long-term stability of the assembled cells could be improved by encapsulation.

In order to verify the effectiveness of the optimized semiconducting networks and the versatility of these production protocols, reference mesoporous TiO_2 based PSCs (mp-TiO_2, see experimental section for details) were also characterized and tested. Although the perovskite morphology is better in the optimized semiconducting networks produced in this work (Fig. S19e and 19f), a markedly improved perovskite morphology consisting of large crystals and reduced pinholes for the mp-TiO_2/$CH_3NH_3PbI_3$ can also be observed upon the mixed solvent (DMF:CBZ=1:1) vapor annealing (Fig. S19b and S19c). The PCE of the mp-TiO_2 device exhibited a ~27% enhancement, increasing from 9.62% (mp-TiO_2) to 12.17% (mp-TiO_2-vapor), Table S4. This shows that the effect of the combined gas-assisted spin coating of the perovskite and the mixed vapor annealing approach increases the conversion efficiency when using different ETLs.

Conclusions

Both the metal oxide and perovskite semiconducting networks within the PSCs have been optimized, and the effect of the ETL particle size and roughness on the subsequent perovskite thin-film deposition was studied. In conjunction with the gas-assisted spin coating method, the mixed vapor annealing approach enabled fabrication of continuous, well-connected and pinhole-free perovskite films with large grain sizes and full surface coverage. The DMF and CBZ play a synergistic role in facilitating the crystal growth, increasing the grain size, densifying the film, smoothing the surface and

improving the crystallinity. As such, the smoothness and the surface coverage of the semiconducting networks have been improved, which has a distinct advantage in improving the device performance and reproducibility. The highest device efficiency based on the optimized semiconducting morphology was 15.77% due to excellent light harvesting, suppressed charge recombination, efficient charge extraction and collection. Importantly, this work demonstrates the ability to tune the crystal growth and evolution of TiO_2 and perovskite by simple wet chemistry and to fabricate uniform semiconducting thin films in a highly controllable manner.

Acknowledgements

The authors acknowledge financial support from the Melbourne Research Grant Support Scheme. The Melbourne Advanced Microscopy Facility at The University of Melbourne provided access to electron microscopy facilities. Support from the Australian Renewable Energy Agency and The Australian Centre for Advanced Photovoltaics is acknowledged. R.A.C. acknowledges the Australian Research Council for a Future Fellowship (FT0990583).

Notes and references

1. M. Grätzel, *Nature Mater.*, 2014, **13**, 838-842.
2. J. Burschka, N. Pellet, S. J. Moon, R. Humphry-Baker, P. Gao, M. K. Nazeeruddin and M. Grätzel, *Nature*, 2013, **499**, 316-319.
3. M. M. Lee, J. Teuscher, T. Miyasaka, T. N. Murakami and H. J. Snaith, *Science*, 2012, **338**, 643-647.
4. J. H. Heo, S. H. Im, J. H. Noh, T. N. Mandal, C. S. Lim, J. A. Chang, Y. H. Lee, H. J. Kim, A. Sarkar, M. K. Nazeeruddin, M. Grätzel and S. I. Seok, *Nature Photon.*, 2013, **7**, 487-492.
5. http://www.nrel.gov/ncpv/images/efficiency_chart.jpg
6. H. P. Zhou, Q. Chen, G. Li, S. Luo, T. B. Song, H. S. Duan, Z. R. Hong, J. B. You, Y. S. Liu and Y. Yang, *Science*, 2014, **345**, 542-546.
7. A. Y. Mei, X. Li, L. F. Liu, Z. L. Ku, T. F. Liu, Y. G. Rong, M. Xu, M. Hu, J. Z. Chen, Y. Yang, M. Grätzel and H. W. Han, *Science*, 2014, **345**, 295-298.
8. N. J. Jeon, J. H. Noh, Y. C. Kim, W. S. Yang, S. Ryu and S. Il Seol, *Nature Mater.*, 2014, **13**, 897-903.
9. L. Zuo, Z. Gu, T. Ye, W. Fu, G. Wu, H. Li and H. Chen, *J. Am. Chem. Soc.*, 2015, **137**, 2674-2679.
10. W.-Q. Wu, F. Huang, D. Chen, Y.-B. Cheng and R. A. Caruso, *Adv. Energy Mater.*, 2016, **6**, 1502027.
11. Y. Yang, K. Ri, A. Y. Mei, L. F. Liu, M. Hu, T. F. Liu, X. Li and H. W. Han, *J. Mater. Chem. A*, 2015, **3**, 9103-9107.
12. Y. Yu, J. Li, D. Geng, J. Wang, L. Zhang, T. L. Andrew, M. S. Arnold and X. Wang, *ACS Nano*, 2015, **9**, 564-572.
13. F. Hao, C. C. Stoumpos, Z. Liu, R. P. H. Chang and M. G. Kanatzidis, *J. Am. Chem. Soc.*, 2014, **136**, 16411-16419.
14. M. Z. Liu, M. B. Johnston and H. J. Snaith, *Nature*, 2013, **501**, 395-398.
15. G. C. Xing, N. Mathews, S. Y. Sun, S. S. Lim, Y. M. Lam, M. Grätzel, S. Mhaisalkar and T. C. Sum, *Science*, 2013, **342**, 344-347.
16. P.-W. Liang, C.-Y. Liao, C.-C. Chueh, F. Zuo, S. T. Williams, X.-K. Xin, J. Lin and A. K. Y. Jen, *Adv. Mater.*, 2014, **26**, 3748-3754.
17. M. D. Xiao, F. Z. Huang, W. C. Huang, Y. Dkhissi, Y. Zhu, J. Etheridge, A. Gray-Weale, U. Bach, Y. B. Cheng and L. Spiccia, *Angew. Chem. Int. Ed.*, 2014, **53**, 9898-9903.
18. N. J. Jeon, J. H. Noh, W. S. Yang, Y. C. Kim, S. Ryu, J. Seo and S. I. Seok, *Nature*, 2015, **517**, 476-480.
19. J.-H. Im, I.-H. Jang, N. Pellet, M. Grätzel and N.-G. Park, *Nature Nanotech.*, 2014, **9**, 927-932.
20. W. Zhang, M. Saliba, D. T. Moore, S. K. Pathak, M. T. Hörantner, T. Stergiopoulos, S. D. Stranks, G. E. Eperon, J. A. Alexander-Webber, A. Abate, A. Sadhanala, S. Yao, Y. Chen, R. H. Friend, L. A. Estroff, U. Wiesner and H. J. Snaith, *Nat. Commun.*, 2015, **6**, 6142.
21. Z. Xiao, Q. Dong, C. Bi, Y. Shao, Y. Yuan and J. Huang, *Adv. Mater.*, 2014, **26**, 6503-6509.
22. G. E. Eperon, V. M. Burlakov, P. Docampo, A. Goriely and H. J. Snaith, *Adv. Funct. Mater.*, 2014, **24**, 151-157.
23. F. Huang, Y. Dkhissi, W. Huang, M. Xiao, I. Benesperi, S. Rubanov, Y. Zhu, X. Lin, L. Jiang, Y. Zhou, A. Gray-Weale, J. Etheridge, C. R. McNeill, R. A. Caruso, U. Bach, L. Spiccia and Y.-B. Cheng, *Nano Energy*, 2014, **10**, 10-18.
24. J. Y. Xiao, Y. Y. Yang, X. Xu, J. J. Shi, L. F. Zhu, S. T. Lv, H. J. Wu, Y. H. Luo, D. M. Li and Q. B. Meng, *J. Mater. Chem. A*, 2015, **3**, 5289-5293.
25. W. Q. Wu, Y. F. Xu, H. S. Rao, H. L. Feng, C. Y. Su and D. B. Kuang, *Angew. Chem. Int. Ed.*, 2014, **53**, 4816-4821.
26. W. Chen, Y. Wu, J. Liu, C. Qin, X. Yang, A. Islam, Y.-B. Cheng and L. Han, *Energy Environ. Sci.*, 2015, **8**, 629-640.
27. G. J. Li, K. L. Ching, J. Y. L. Ho, M. Wong and H. S. Kwok, *Adv. Energy. Mater.*, 2015, **5**, 1401775.
28. W. Q. Wu, F. Z. Huang, D. H. Chen, Y. B. Cheng and R. A. Caruso, *Adv. Funct. Mater.*, 2015, **25**, 3264-3272.
29. Y. Chen, T. Chen and L. Dai, *Adv. Mater.*, 2015, **27**, 1053-1059.
30. C. Bi, Y. Yuan, Y. Fang and J. Huang, *Adv. Energy Mater.*, 2015, **5**, 1401616.
31. W. Nie, H. Tsai, R. Asadpour, J.-C. Blancon, A. J. Neukirch, G. Gupta, J. J. Crochet, M. Chhowalla, S. Tretiak, M. A. Alam, H.-L. Wang and A. D. Mohite, *Science*, 2015, **347**, 522-525.
32. T. Baikie, Y. N. Fang, J. M. Kadro, M. Schreyer, F. X. Wei, S. G. Mhaisalkar, M. Grätzel and T. J. White, *J Mater Chem A*, 2013, **1**, 5628-5641.
33. W. Q. Wu, H. L. Feng, H. S. Rao, Y. F. Xu, D. B. Kuang and C. Y. Su, *Nat. Commun.*, 2014, **5**, 3968.
34. J. You, Z. Hong, Y. Yang, Q. Chen, M. Cai, T.-B. Song, C.-C. Chen, S. Lu, Y. Liu and H. Zhou, *ACS Nano*, 2014, **8**, 1674-1680.
35. H. J. Snaith, A. Abate, J. M. Ball, G. E. Eperon, T. Leijtens, N. K. Noel, S. D. Stranks, J. T. W. Wang, K. Wojciechowski and W. Zhang, *J. Phys. Chem. Lett.*, 2014, **5**, 1511-1515.
36. R. S. Sanchez, V. Gonzalez-Pedro, J. W. Lee, N. G. Park, Y. S. Kang, I. Mora-Sero and J. Bisquert, *J. Phys. Chem. Lett.*, 2014, **5**, 2357-2363.
37. Y. Shao, Z. Xiao, C. Bi, Y. Yuan and J. Huang, *Nat. Commun.*, 2014, **5**, 5784.
38. C. Zhao, B. Chen, X.Qiao, L. Luan, K. Lu and B. Hu, *Adv. Energy Mater.*, 2015, **5**, 1500279.

Title: Optimizing semiconductor thin films with smooth surfaces and well-interconnected networks for high-performance perovskite solar cells

Table of Contents:

Combined hydrothermal treatment, gas-assisted spin coating and mixed vapor annealing approaches can effectively optimize the semiconducting networks in thin film perovskite photovoltaic devices. Perovskite solar cells consisting of a smooth metal oxide electron transport layer and a compact, pinhole-free $CH_3NH_3PbI_3$ layer attain power conversion efficiencies as high as 15.77% owing to efficient light harvesting, suppressed charge recombination and effective charge extraction in the bilayer structure.